

# Regulation Mechanism for the Binding between the SARS-CoV-2 Spike Protein and Host Angiotensin-Converting Enzyme II

Haiyi Chen, Yu Kang, Mojie Duan,\* and Tingjun Hou\*



Cite This: *J. Phys. Chem. Lett.* 2021, 12, 6252–6261



Read Online

ACCESS |



Metrics & More

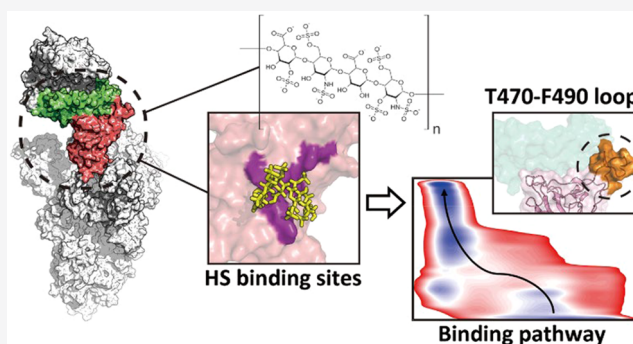


Article Recommendations



Supporting Information

**ABSTRACT:** Severe acute respiratory syndrome coronavirus 2 (SARS-CoV-2) infection is mainly mediated through the interaction between the spike protein (S-pro) of the virus and the host angiotensin-converting enzyme II (ACE2). The attachment of heparan sulfate (HS) to S-pro is necessary for its binding to ACE2. In this study, the binding process of the receptor-binding domain (RBD) of S-pro to ACE2 was explored by enhanced sampling simulations. The free-energy landscape was characterized to elucidate the binding mechanism of S-pro to ACE2 with and without HS fragment DP4. We found that the stability of the T470-F490 loop and the hydrophobic interactions contributed from F486/Y489 in the T470-F490 loop of S-pro are quite crucial for the binding, which is enhanced by the presence of DP4. Our study provides valuable insights for rational drug design to prevent the invasion of SARS-CoV-2.



The severe acute respiratory syndrome coronavirus 2 (SARS-CoV-2) has been rapidly spreading all over the world since December 2019.<sup>1</sup> The coronavirus disease 2019 (COVID-19) induced by the invasion of SARS-CoV-2 has led to more than 100 million infected patients and over two million deaths up to March 2021. Currently, no proven effective medications or therapy options are available for the treatment of the fatal contagious disease.<sup>2,3</sup> Meanwhile, the fast evolution of the virus induced stronger infection ability and/or higher toxicity (e.g., the N501Y mutated<sup>4,5</sup> and D614G mutated strains<sup>6–10</sup>), which raises great challenges for combating the virus.

The study of the infection mechanism and the regulation on the invasion process can greatly improve the understanding of the pathogenesis and the development of antiviral drugs. The infection of the virus to host is initiated by the interactions between SARS-CoV-2 spike protein (S-pro) and host cell surface receptors.<sup>11</sup> S-pro is constituted of two subdomains (S1 and S2) and always presents as a trimer on the surface of coronaviruses.<sup>12,13</sup> The receptor binding domain (RBD) positioned in S1 of S-pro can bind to angiotensin-converting enzyme II (ACE2) on host cells.<sup>14,15</sup> Many efforts have been devoted to investigate the interaction between SARS-CoV-2 S-pro and ACE2. The structure details of the binding interface between the S-pro RBD and ACE2 has been identified by crystallography,<sup>16–18</sup> and the interaction surface of S-pro can be divided into three contact regions, i.e., CR1, CR2, and CR3.<sup>19</sup> It was proposed that the polar interactions between CR2 of the S-pro RBD and human ACE2 (hACE2) provide large contributions to the binding of the SARS-CoV-2 S-pro

RBD.<sup>20–23</sup> Moreover, the conformational changes of the RBD to an open state would enhance its interactions with ACE2 and facilitate the S-pro-ACE2 association.<sup>11,24–26</sup> However, the detailed interactions and structure dynamics, as well as the important intermediate states of SARS-CoV-2 S-pro in the binding process with hACE2, remain unclear.

In addition, the binding process and binding affinity of SARS-CoV-2 with ACE2 are regulated by glycoconjugates.<sup>27</sup> Glycan and glycoconjugates spread all over host cells, and they are usually utilized as the attachments in the initial stage of infection for many viral pathogens. Heparan sulfate (HS), which is a highly negatively charged linear polysaccharide attaching to the cell membrane and extracellular matrix proteoglycans,<sup>28</sup> was found to play critical roles in the infection of coronaviruses,<sup>29</sup> including SARS-CoV-1 and MERS-CoV.<sup>30</sup> The recent studies showed that the interaction between the S-pro RBD and the HS attached on the host cell membrane is quite essential for the binding of the SARS-CoV-2 S-pro trimers to ACE2.<sup>31–34</sup> By investigating the SARS-CoV-2 virus infection ratio to the human bronchial epithelial cells, Clausen et al. reported that a dramatic decrease of infection was observed in the HSase-treated cells, which demonstrates

Received: May 14, 2021

Accepted: June 28, 2021



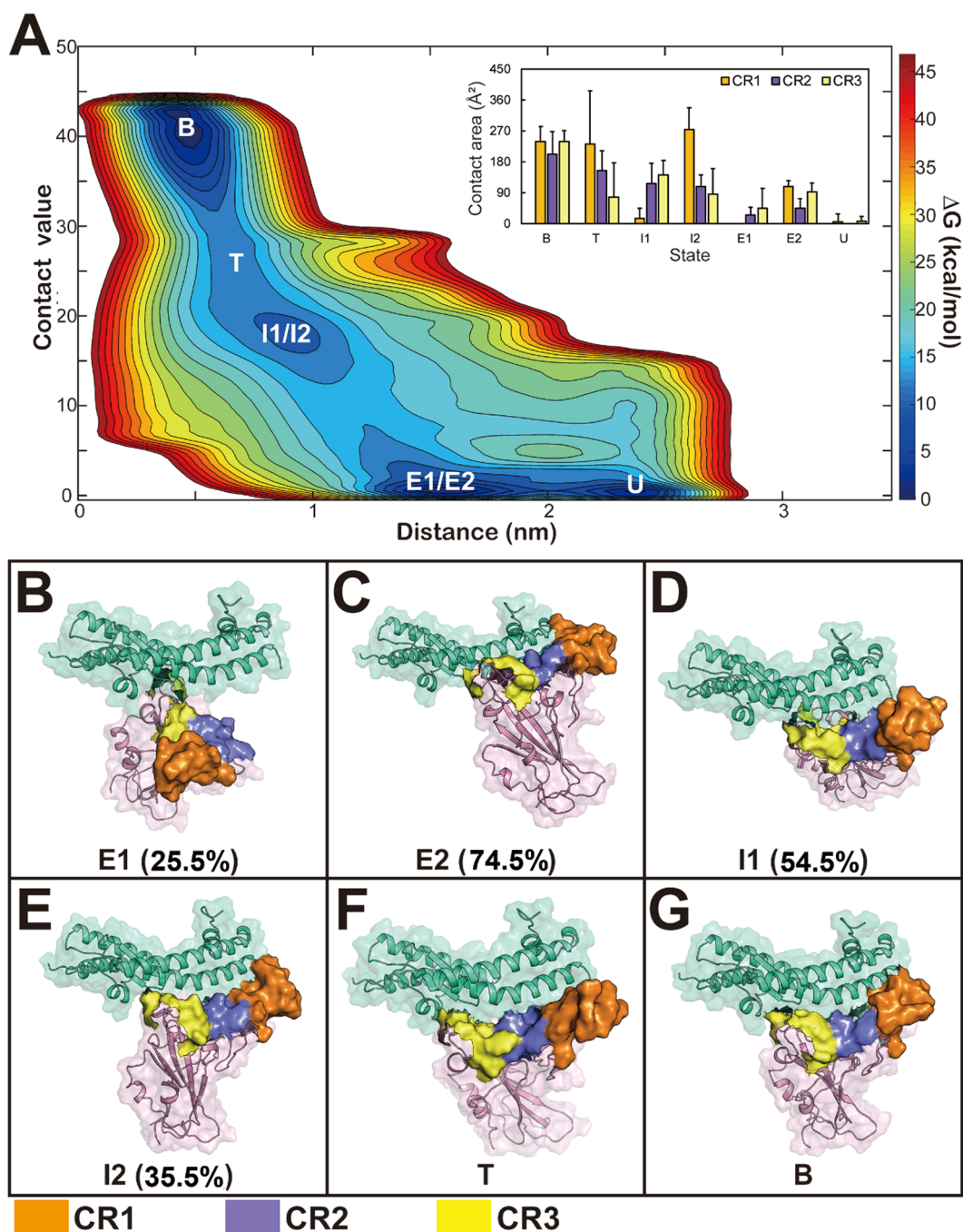


**Figure 1.** Binding process between the S-pro RBD and ACE2. (A) Two-dimensional free-energy surface of the binding process. The contact areas of CR1, CR2, and CR3 in different states were calculated and are shown in the inset. (B–G) Representative conformations of different states. In each representative conformation, ACE2 and S-pro are colored in green and pink, respectively. The CR1, CR2, and CR3 on S-pro are represented by surfaces and are colored in brown, purple, and yellow, respectively. The populations of different modes in the states are given.

the crucial role of HS in the virus infection.<sup>31</sup> The understanding of the regulation mechanism of HS to the S-pro RBD binding would provide important information for the development of effective therapies for COVID-19.

In this study, we focus on the following three questions which are important to the binding process of SARS-CoV-2 S-pro to hACE2: (1) What are the predominant intermediates and stages in the binding process? (2) Are there other important interactions in the binding process except the polar interactions between CR2 and hACE2? (3) How is the binding regulated by the endogenic molecules such as HS? To answer

these questions, all-atom molecule dynamics (MD) simulations and enhanced sampling methods were employed to study the binding process between S-pro and ACE2. The free-energy landscapes of the binding process with/without the attachment of HS were constructed. The results suggest multiple stages in the binding process, with the polar interactions dominant in the initial association. Moreover, the hydrophobic interactions between a few residues in CR1 and ACE2 are found crucial for the formation of the binding intermediates. The presence of the heparan molecules would stabilize the CR1 structure and facilitate the hydrophobic interactions, which could decrease

the free-energy barrier to form the final complex. The binding mechanism revealed by this study improves our understanding of SARS-CoV-2 infections and would greatly help the development of vaccines and drugs to combat COVID-19.

To characterize the binding mechanism between SARS-CoV-2 S-pro and hACE2, the enhanced sampling method was employed to generate the free-energy landscape along the important reaction coordinates describing the binding process. The two-dimensional free-energy landscape as a function of the center-of-mass (COM) distance between the backbone heavy atoms of the two proteins at the binding interface and the native contacts of the selected residue pairs was constructed (Figure 1). The details of the enhanced sampling simulations and the set of the reaction coordinates are described in Computational Methods in the Supporting Information. Several free-energy minima were observed along the binding process, i.e., the unbound state (state U), the encounter complex (state E), the intermediate (state I) with about half of native contacts formed, the transition state (state T), and the fully bound state (state B). The representative conformations of the above states are given in Figure 1. In order to describe the features of the binding process, the binding interface on the RBD of S-pro is divided into three regions, two of which are located at the ends of the binding interface, named as CR1 (residues E471-Y489) and CR3 (residues G446-Y451 and Y495-G502), and the middle region is denoted as CR2 (residues K417, L452-F456, and F490-S494).<sup>19</sup> The locations of the three regions on S-pro are illustrated in Figure S1.

Considering the free-energy landscape, the binding process can be divided into three stages: from the unbound state U to the encounter complex E, from the encounter complex to the intermediate state I, and from the intermediate state to the complete bound state B. The encounter complex corresponds to the initial touch of the two proteins. Two interacting modes are observed in the encounter complex of S-pro with ACE2. In the first mode (E1), only the S-pro CR3 contacts with ACE2, while in the second mode (E2), both CR1 and CR3 contact with ACE2. E2 dominates the early stage binding, about 75% conformations of the encounter complex state are observed in this mode, compared with around 25% conformations observed in the mode E1. The contact surface area analysis (Figure 1A insertion) shows that the contacts between CR3 and ACE2 are predominant (64.3%) in the state E1, with an average contact area on CR3 of 44.2 Å<sup>2</sup>. But in E2, the interactions between CR1/CR3 and ACE2 contribute more to the binding, with the average contact areas on CR1 and CR3 of 108.1 and 92.6 Å<sup>2</sup>, respectively. The contributions of the interactions between ACE2 and CR2 are relatively low in both E1 and E2 (24.5 and 43.9 Å<sup>2</sup>, respectively).

The native contact values of the structures in the encounter complex are close to zero, suggesting that the non-native interactions drive the initial approach of S-pro to ACE2. More contacts including the native contacts form in the intermediate state than the encounter complex. There are also two interacting modes (I1 and I2) in the intermediate state. CR2 and CR3 of S-pro are involved in the binding in the interaction mode 1 (I1), and the average binding areas of these two regions are 115.9 and 141.3 Å<sup>2</sup>, respectively. The structures of I1 might proceed from the structures of the encounter-complex E1 because the CR1 region is far from ACE2 in both E1 and I1. In the second interacting mode of the intermediate state (I2), the structures with all the CR regions interact with ACE2. CR1 has the largest average contact area (273.6 Å<sup>2</sup>)

with ACE2. Compared with the structures in the encounter-complex E2, the binding positions of S-pro are adjusted to adopt more native contacts with ACE2.

Considering the free-energy surface and the features of the structures in the free-energy minima, we propose that there are probably two different pathways for the binding of S-pro to ACE2. Pathway 1 is along U → E1 → I1 → T → B, and pathway 2 is along U → E2 → I2 → T → B. Although the population of pathway 2 is dominant in the early stage of the binding (i.e., the formation of the encounter complex), the structures in the intermediate states along the two different pathways are comparable (54.5% in I1 vs 45.5% in I2).

The binding of HS would change the structures of S-pro and promote the interactions between S-pro and ACE2, which is important to the infection of SARS-CoV-2. The binding sites of HS on S-pro still need further identification.<sup>31</sup> In this study, GlcA(2S)-GlcNS(6S)-GlcA-GlcNS(3, 6S) (DP4) was employed to study the possible HS binding sites on S-pro. Heparin is a kind of polysaccharide sharing characteristic similar to HS, both of which are constituted by repeated disaccharides covalently linked by uronic acid and acetylglucosamine.<sup>35</sup> Heparin has been applied as an anticoagulant, and recently, it was found that heparin can bind to the RBD domain of the SARS-CoV-2 S-pro trimer and increase the percentage of the S1 subunits occupied by ACE2.<sup>31</sup> The unbiased MD simulations were conducted to analyze the possible binding positions of DP4 on S-pro, and a total of 100 replicas of the MD simulations (100 ns each) with random initial positions of DP4 were performed. The last frames of 100 ns MD simulation trajectories were used to show the positions of DP4 around S-pro. The binding between DP4 and S-pro is more stable in site I than in other sites; no separation from site I after binding was observed in our simulations.

Four possible binding sites of DP4 on S-pro were observed (Figure 2). The most populated binding site (site I) is enriched with positively charged residues, including R355, K356, R357, and R466, which were also reported in the previous study.<sup>31</sup> About one-third of DP4 bind within site I. The binding of DP4 to site I on S-pro is the most populated one because of the strong electrostatic interactions. Site II (residues 457–459) and site III (residues 446, 447, 449, 496, and 498) are less populated, which are located close to CR1 and CR3 of S-pro, respectively (Figures 2 and S1). Fewer positively charged residues are observed in the binding sites compared with site I (two in site II or IV and zero in site III), and the binding of DP4 to these three sites is unstable. The binding sites I, II, and IV (residues 346 and 509) are also observed by a previous molecule docking work.<sup>31</sup> It should be noted that site I has large binding space for the negatively charged heparin, which would also facilitate the contact between this site and longer heparin units.

To investigate the regulation of the heparin molecule to the binding of S-pro to ACE2, 400 ns metadynamics simulations were performed on the DP4-bound S-pro and ACE2. Compared with the DP4-absent system, the presence of DP4 promotes the conformational space shifting toward the bound state of the S-pro-ACE2 complex. There is only one dominant low free-energy pathway for the binding between S-pro/DP4 and ACE2 (Figure 3A). The free-energy difference between the fully bound state B and the unbound state is about 8 kcal/mol based on the one-dimensional free-energy profile (Figure S2), which is much larger than that in the absence of DP4. These results demonstrate that DP4 could increase the binding

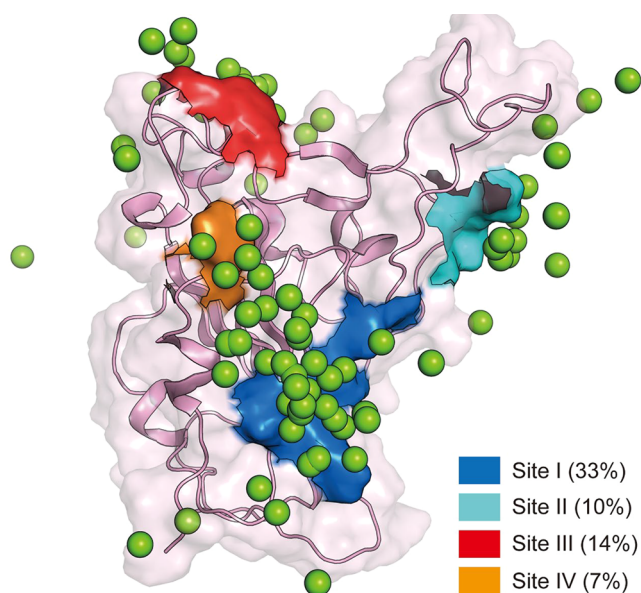


**Figure 2.** Positions of DP4 in the final snapshots of the 100-replica unbiased MD simulation trajectories. The centers of DP4 are represented by the green spheres. The RBD of SARS-CoV-2 is drawn as a pink cartoon covered with light pink surface. Four major binding sites, i.e., site I, site II, site III, and site IV, are colored in blue, cyan, red, and orange, respectively. The appearance ratios of these binding sites are given.

affinity of S-pro to ACE2, which is consistent with experimental observations.<sup>31</sup>

The binding process of S-pro/DP4 to ACE2 can also be divided into three stages, i.e., the unbound state (U) to the encounter complex (E), the encounter complex to the binding intermediate (I), and the binding intermediate to the complete bound state (B). Although two separated free-energy minima (E1 and E2) are observed in the encounter complex region, the approaching of S-pro to ACE2 is induced by the interactions between CR3 and ACE2 in both E1 and E2 (Figure 3B,C). The structures in the encounter complex E1 (Figure 3B) are similar to those in the E1 of the binding of apo-S-pro to ACE2 (Figure 1B), in which the non-native contacts dominate the interactions between these two proteins. The structures in the encounter complex E2 are more compact, and several native contacts are formed. However, only one major interacting mode in the stage of the encounter complex formation was observed, i.e., CR3 of S-pro contacting with ACE2.

Similar to the encounter complex of S-pro/DP4 and ACE2, there is also only one single interacting mode in the intermediate I (Figure 3E). All three regions (CR1, CR2, and CR3) on the binding interface between S-pro and ACE2 (the contact areas on the three regions are 152.8, 227.8, and 246.7 Å<sup>2</sup>, respectively), but some native contacts are missing in state I. By adjusting the conformations of the residue side-chains and the interactions on the binding interface of the structures in the state I, the complex would form the final bound state (state B). The free-energy minimum O has small COM distances between S-pro and ACE2, but the native contacts formed in this state are lower than those in state I. Compared with the crystal structure,<sup>16</sup> the orientation of S-pro in state O is deviated from that in the complex structure. We infer that the free-energy minimum O is an off-pathway state of the binding process.

The major free-energy barrier located at the COM distance around 1.0 nm can be observed in both systems (Figure S2), which suggests the critical step from the encounter complex to the intermediates regardless of the presence or absence of DP4. However, the free-energy barrier from the intermediate states to the bound state is much lower in the presence of DP4 than in the absence of DP4 (about 2 kcal/mol in S-pro/DP4-ACE2 and 10 kcal/mol in apo-S-pro-ACE2 in Figure S2).

The structures of S-pro in the systems with/without DP4 were compared. The structure fluctuations in the different regions of S-pro in both systems were calculated for the conformations in each state and are given in Figures 4 and S3. The flexibility in most regions is not affected by the binding of DP4 to S-pro, even in the DP4 binding sites. However, the CR1 structure in the S-pro RBD is much more stable in the presence of DP4, even in the U states. The average heavy atom root-mean-square-fluctuation (RMSF) values of CR1 (including the residues 476–478 and 481–486) are 3.0 and 9.6 Å for states U and B of the DP4-absent system, respectively, while those of the DP4-present system are reduced to 1.2 and 2.1 Å, respectively.

Further structure analysis shows that the flexibility of CR1 is related to the hydrogen bond between Y473 and Y489, which would stabilize the  $\beta$ -sheet in CR1. In the presence of DP4, more than one stable hydrogen bond would form between the backbone atoms of Y473 and Y489. The occupancies of the hydrogen bonds between Y473 and Y489 in the on-pathway minima are 86.1% (state U), 94.7% (state I), and 88.5% (state B), respectively. The formation of these hydrogen bonds is believed to stabilize the structure of CR1, with the largest RMSF values of the CR1-atoms in states U, I, and B of 3.2, 4.2, and 3.0 Å, respectively. In contrast, without DP4, the largest RMSF values are up to 16.1 Å (state U), 10.1 Å (state I), and 8.1 Å (state B), respectively. Meanwhile, the hydrogen bond occupancies of Y473–Y489 in the unbound state (state U), intermediates (state I), and encounter complexes (state E) are reduced to 43.2%, 52.3%, and 18.7%, respectively.

In order to illuminate the atom-level binding mechanism of S-pro to ACE2, the residue interactions in the different stages of the binding processes were analyzed. The interactions in the bound states of both systems (i.e., S-pro with ACE2 and S-pro/DP4 with ACE2) are basically identical to those in the crystal structure and previously reported results.<sup>19</sup> The interactions between S-pro and ACE2 could be divided into three classes based on the locations and types of the binding residues, denoted as the hydrophobic cluster, polar contact network I, and polar contact network II (Figure 5A). The hydrophobic cluster mainly includes the residues L455, F456, F486, and Y489 in CR1 of S-pro and F28, M82, Y83, and H34 in ACE2. The polar interaction network I is composed of the hydrophilic residues in CR3 on the S-pro and ACE2 binding interface. The residues K353 in ACE2 and Q498 in S-pro are the hubs in the interaction network. The polar interaction network II mainly contains residues on the binding interface between CR2 of S-pro and ACE2, and Q493 plays the central role in the interactions. The residue and atom composition of the connections are given in Figure 5B and Table S1.

The highest free-energy barriers along the binding process are located between the encounter-complex and the intermediates, and therefore, the rearrangement of the residue interactions in this step are important for the binding. The greatest changes from the state E1/E2 to state I are the formation of the hydrophobic interactions related to CR1 of S-

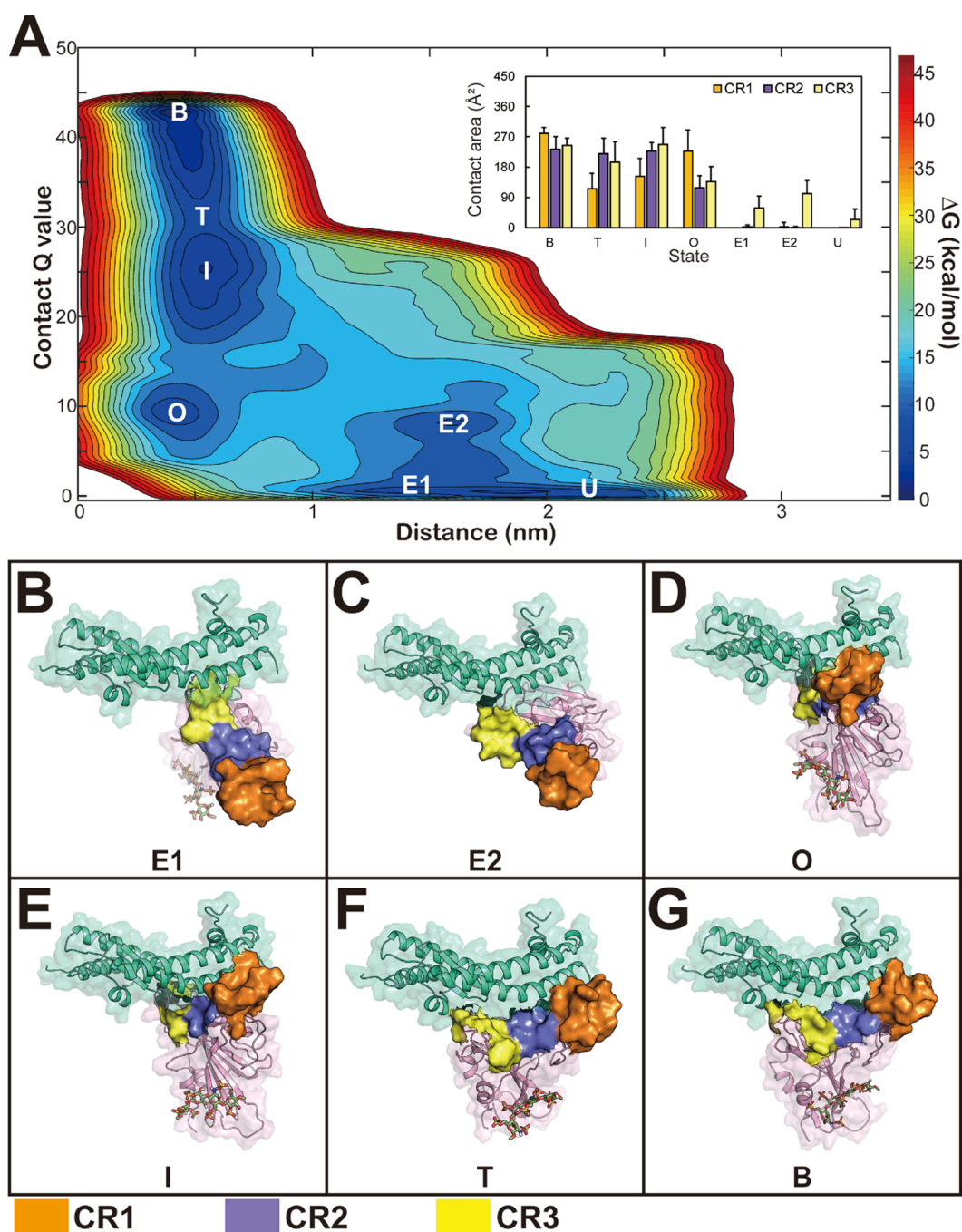


**Figure 3.** Binding process between the S-pro RBD and ACE2 in the presence of DP4. (A) Two-dimensional free-energy surface of the binding process. The contact areas of CR1, CR2, and CR3 in different states are given in the inset. (B–G) Representative conformations of different states. The colors and representations of proteins are the same as in Figure 1, and DP4 is shown as a stick model.

pro, especially the hydrophobic cluster formed by the residues F486/Y489 in S-pro and F28/L79 in ACE2. The formation of the hydrophobic cluster should be the rate-limiting step for the binding process, and the free-energy barrier is largely contributed from the entropy cost induced by the flexibility of CR1 (Figure 4C). The transitions from the intermediate state to the fully bound state B would be a faster step because there is no energy obstruction to reach the state B. Our results are consistent with the recent cryo-EM studies on the complex structure of the ACE2-bound SARS-CoV-2 S-trimer,<sup>25</sup> which found that the hydrophobic interactions with the involvement of F486/Y489 in the T470-F490 loop of S-pro are important

to the complex formation. More importantly, we found that the hydrophobic interactions mainly contribute to the transitions from the encounter-complex to intermediate instead of the initial encountering of the binding.

To investigate how the DP4 molecules regulate the binding of S-pro to ACE2, the interactions between S-pro and ACE2 in the early stages of the binding processes (i.e., the encounter complex) were analyzed. Several non-native polar interactions formed between S-pro and ACE2 in both the DP4-present/absent systems, indicating that the polar interactions provide the initial driven force for the approach of S-pro to ACE2 (Figure S4). On the other side, the hydrophobic interactions

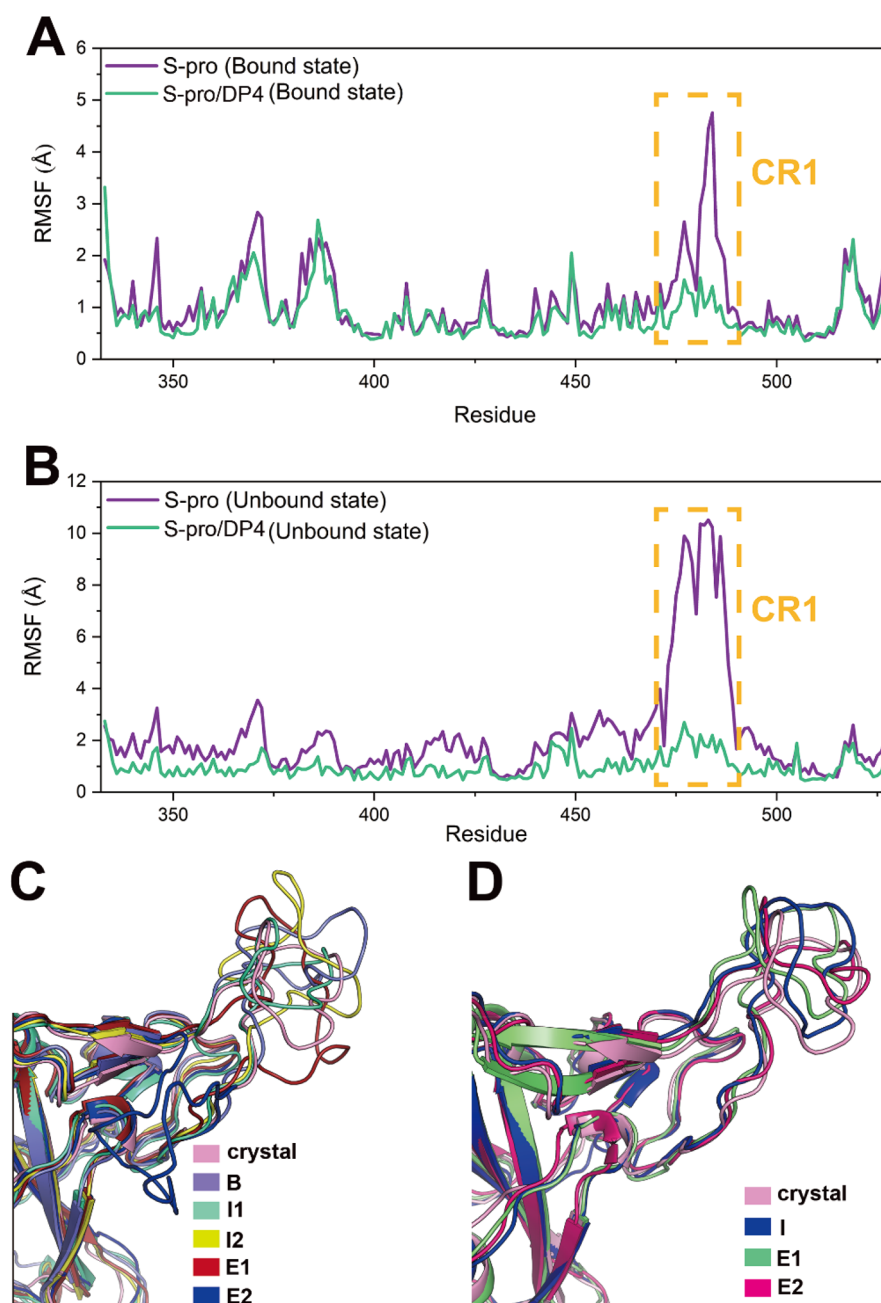


**Figure 4.** Structure fluctuation of S-pro in the binding process. (A) Heavy atom RMSFs of the structures in bound states. The residues in CR1 (T470-F490 loop) are labeled by the yellow dashed frame. (B) Heavy atom RMSFs of the structures in unbound states. The CR1 residues (T470-F490 loop) are labeled by the yellow dashed frame. (C) Representative conformations of S-pro CR1 in different states of the binding process of apo-S-pro and ACE2. (d) Representative conformations of S-pro CR1 in different states of the binding process of S-pro/DP4 and ACE2.

constituted by residues in CR1 of S-pro and ACE2 are different in the intermediate states of the two systems. In the presence of DP4, CR1 of S-pro is restrained by the electrostatic interaction between the negatively charged sulfuric acid group on DP4 and the positively charged residue R466. Therefore, the hydrophobic residues F456, Y473, F486, and Y489 in S-pro would form a native hydrophobic cluster which further facilitates the interactions between S-pro and ACE2. However, in the DP4-absent case, CR1 on S-pro is unstable and a non-native hydrophobic cluster including V483 in the S-pro RBD would form (Figures S4 and S5) in the early stage, which impedes the transformation from the encounter complex to the final bound complex.

Many polar interactions are important for the transitions from the intermediate to the bound complex, including the residues D30 and E35 in ACE2 and R403, K417, and Q493 in S-pro. In the intermediate state, very few hydrogen bonds formed between Q493 and E35 and between K417 and D30. The occupancies of the hydrogen bonds in Q493(S-pro)-E35(ACE2) and K417(S-pro)-D30(ACE2) in the intermediate are 21.0% and 18.4%, respectively. More than half of the conformations in the bound state possess these two hydrogen bonds, indicating that the interactions are important to the stability of the S-pro-ACE2 complex. It should be noted that in a recent study K417 was found to be a key residue in the virus infection and the binding of neutralizing antibodies.<sup>36</sup>

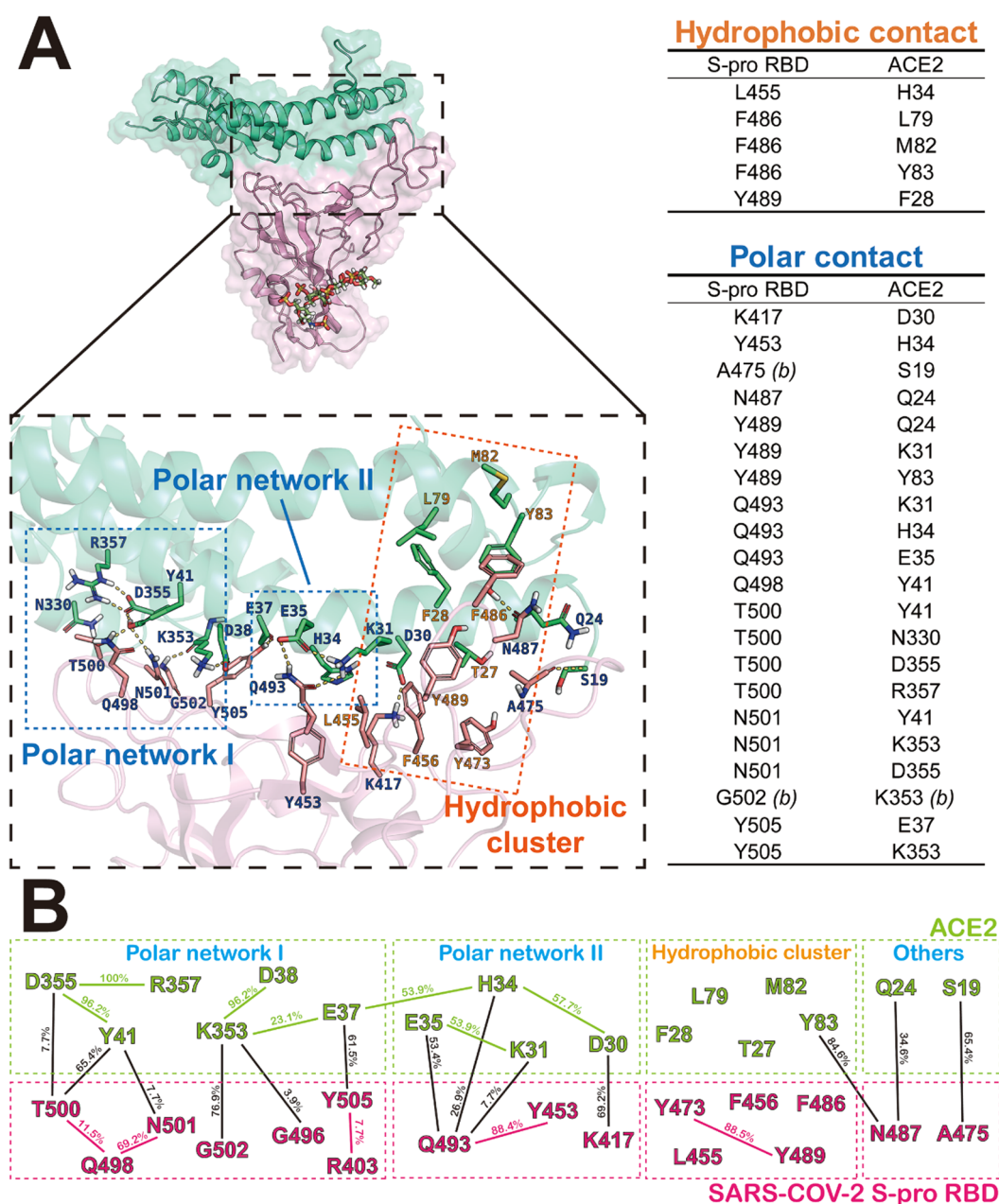


**Figure 5.** Interactions between S-pro and ACE2 in the bound state of system with DP4. (A) Residues in the interaction interface of the conformation in the bound state. The contact residue pairs (cutoff = 5.5 Å) with occupancies higher than 90% are listed in the figure. The interaction networks in different regions are labeled. (B) Interaction networks between RBD and ACE2. The residues on S-pro are colored in red, while those in ACE2 are colored in green. The percentages of the hydrogen bonds are labeled on the lines between two residues.

Interestingly, the residue D30 in ACE2 prefers to form a stable non-native hydrogen bond with R403 in S-pro in the intermediate state (occupancy of 81.6%). The system needs to overcome the free-energy barrier related to the breaking of the hydrogen bond between R403 and D30 to reach the bound state from the intermediate.

Recently, public concerns have been raised regarding the more contagious mutations P.1 in South Africa (K417N-E484K-N501Y) and B.1.351 in Brazil (K417T-E484K-N501Y). On the basis of reported experimental and computational results, the mutation E484K is considered crucial for stronger binding affinity to ACE2.<sup>37,38</sup> The binding conformation of the P.1 variant S-pro RBD and ACE2 (PDB: 7NXC) is highly similar (RMSD = 0.30 Å) to that of wild-type

S-pro RBD and ACE2 (PDB: 6LZG). In the crystal structure 7NXC, the side chain of mutated K484 is placed at the same position of the original E484; however, instead of the original negative electrostatic surface of E484, the positive electrostatic surface of K484 provides polar interaction with E35 in ACE2.<sup>38</sup> Our results are consistent with this conclusion and further suggest a faster binding process between E484K S-pro RBD and ACE2. In the intermediate state of the supposed “naturally” binding process with the presence of DP4, an exclusive polar contact between RBD-E484 and ACE2-E75 (>90%, Figure 6A), together with the non-native polar interaction between RBD-E484 and ACE2-K68 (65.4%, Figure 6B), was observed, suggesting E484 should be an obstruction

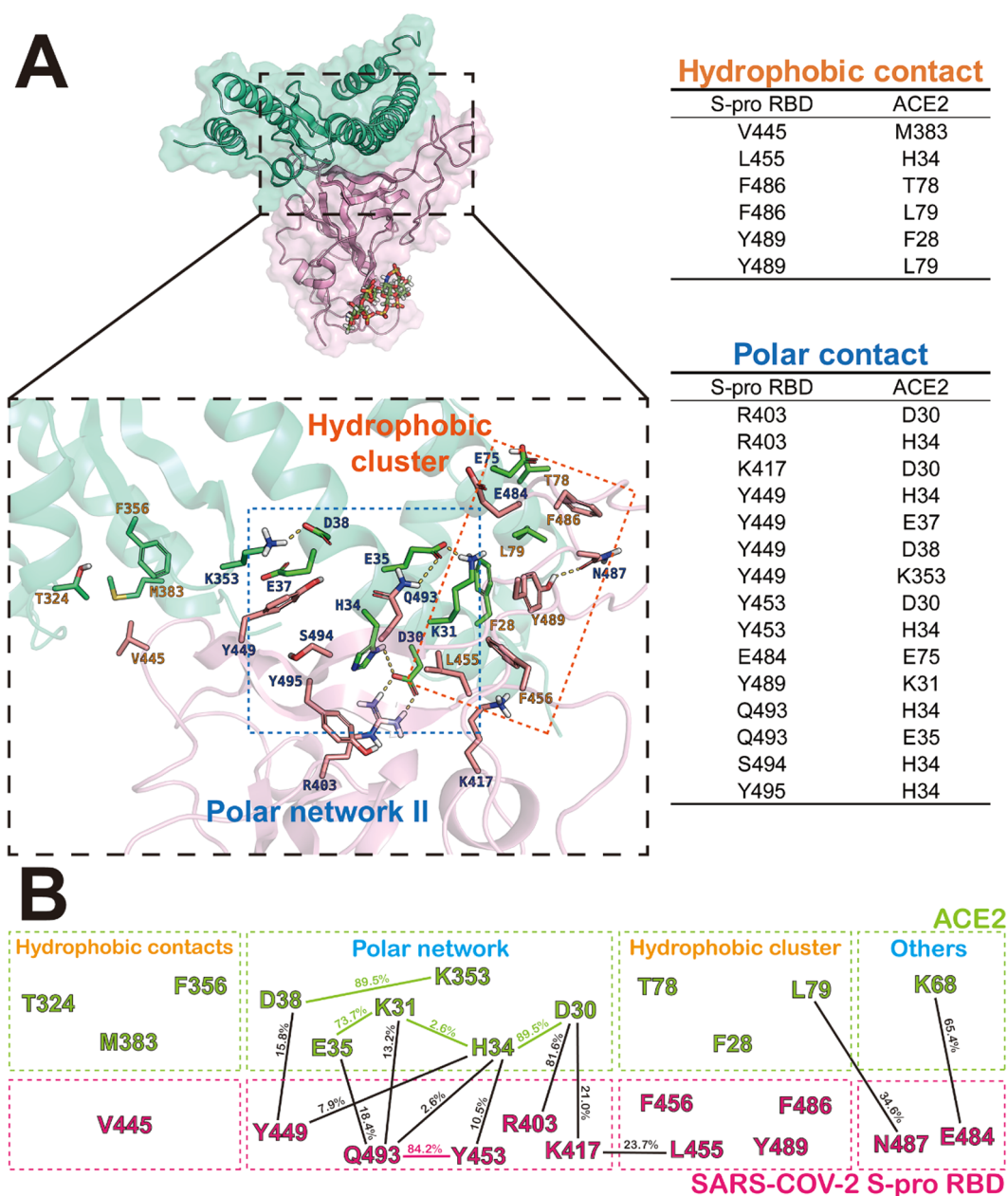


**Figure 6.** Interactions between S-pro and ACE2 in the intermediate state of the system with DP4. (A) Residues in the interaction interface of the conformation in the intermediate state. The contact residue pairs (cutoff = 5.5 Å) with occupancies higher than 90% are listed in the figure. The interaction networks in different regions are labeled. (B) Interaction networks between S-pro and ACE2 in the intermediate state.

for the formation of the final interaction network between RBD-CR1 and ACE2.

In conclusion, the binding processes and binding free-energy landscape of the S-pro RBD with ACE2 were characterized in this study. Multiple stages were observed in the binding process of S-pro to ACE2, i.e., from the unbound state (U) to the encounter complex (E), followed by the intermediate, and finally to the bound complex. The formation of the encounter complex is mainly driven by the polar interactions between the two proteins. In addition, the hydrophobic interactions between ACE2 and CR1 of S-pro (i.e., the T470-F490 loop) are crucial for the system transitions to the intermediate from the encounter complex. The binding of SARS-CoV-2 S-pro with ACE2 is facilitated by glycoconjugates. The binding of DP4 mostly affects the structure of CR1 (T470-F490 loop). In the DP4-absent system, CR1 of S-pro is more flexible in the

unbound state and encounter complex during the binding process compared with that in the DP4-present system. Moreover, the presence of DP4 would rearrange the inner interactions of S-pro and stabilize the T470-F490 loop, which facilitates the interactions between the hydrophobic residues in S-pro and ACE2. Our results give the detailed mechanism and regulation of the binding of S-pro to ACE2, which improve our understanding of SARS-CoV-2 infections and will be a great help for the development of vaccines and drugs against COVID-19.

## ■ ASSOCIATED CONTENT

### Supporting Information

The Supporting Information is available free of charge at <https://pubs.acs.org/doi/10.1021/acs.jpclett.1c01548>.

Computational details; lists of hydrogen bond formation; additional figures showing different regions in binding interface, 1D free-energy profiles of binding, structure fluctuation of S-pro, interactions in encounter complex state, interactions between T470-f490 loop and ACE2, COM distances as a function of simulation time, and convergence tests of metadynamics (PDF)

## AUTHOR INFORMATION

### Corresponding Authors

**Mojie Duan** – National Centre for Magnetic Resonance in Wuhan, State Key Laboratory of Magnetic Resonance and Atomic and Molecular Physics, Innovation Academy for Precision Measurement Science and Technology, Chinese Academy of Sciences, Wuhan 430071, Hubei, China; [orcid.org/0000-0002-5496-832X](https://orcid.org/0000-0002-5496-832X); Email: [mjduan@wipm.ac.cn](mailto:mjduan@wipm.ac.cn)

**Tingjun Hou** – Hangzhou Institute of Innovative Medicine, College of Pharmaceutical Sciences and State Key Lab of CAD&CG, Zhejiang University, Hangzhou 310058, Zhejiang, China; [orcid.org/0000-0001-7227-2580](https://orcid.org/0000-0001-7227-2580); Email: [houtingjun@zju.edu.cn](mailto:houtingjun@zju.edu.cn)

### Authors

**Haiyi Chen** – National Centre for Magnetic Resonance in Wuhan, State Key Laboratory of Magnetic Resonance and Atomic and Molecular Physics, Innovation Academy for Precision Measurement Science and Technology, Chinese Academy of Sciences, Wuhan 430071, Hubei, China; Hangzhou Institute of Innovative Medicine, College of Pharmaceutical Sciences, Zhejiang University, Hangzhou 310058, Zhejiang, China

**Yu Kang** – Hangzhou Institute of Innovative Medicine, College of Pharmaceutical Sciences, Zhejiang University, Hangzhou 310058, Zhejiang, China

Complete contact information is available at:

<https://pubs.acs.org/10.1021/acs.jpclett.1c01548>

### Notes

The authors declare no competing financial interest.

## ACKNOWLEDGMENTS

This work is funded by National Natural Science Foundation of China (21773298), Key R&D Program of Zhejiang Province (2020C03010), and Zhejiang Provincial Natural Science Foundation of China (LZ19H300001).

## REFERENCES

- (1) Zhu, N.; Zhang, D. Y.; Wang, W. L.; Li, X. W.; Yang, B.; Song, J. D.; Zhao, X.; Huang, B. Y.; Shi, W. F.; Lu, R. J.; Niu, P. H.; Zhan, F. X.; Ma, X. J.; Wang, D. Y.; Xu, W. B.; Wu, G. Z.; Gao, G. F.; Tan, W. J.; Coronavirus, C. N. A Novel Coronavirus from Patients with Pneumonia in China, 2019. *N. Engl. J. Med.* **2020**, *382* (8), 727–733.
- (2) Beigel, J. H.; Tomashek, K. M.; Dodd, L. E. Remdesivir for the Treatment of Covid-19-Preliminary Report REPLY. *New Engl J. Med.* **2020**, *383* (10), 992–994.
- (3) Jiang, Y. W.; Chen, D. Q.; Cai, D.; Yi, Y.; Jiang, S. Effectiveness of remdesivir for the treatment of hospitalized COVID-19 persons: A network meta-analysis. *J. Med. Virol.* **2021**, *93* (2), 1171–1174.
- (4) Leung, K.; Shum, M. H. H.; Leung, G. M.; Lam, T. T. Y.; Wu, J. T. Early transmissibility assessment of the N501Y mutant strains of SARS-CoV-2 in the United Kingdom, October to November 2020. *Eurosurveillance* **2021**, *26* (1), 15–21.
- (5) Gu, H. J.; Chen, Q.; Yang, G.; He, L.; Fan, H.; Deng, Y. Q.; Wang, Y. X.; Teng, Y.; Zhao, Z. P.; Cui, Y. J.; Li, Y. C.; Li, X. F.; Li, J. F.; Zhang, N. N.; Yang, X. L.; Chen, S. L.; Guo, Y.; Zhao, G. Y.; Wang, X. L.; Luo, D. Y.; Wang, H.; Yang, X.; Li, Y.; Han, G. C.; He, Y. X.; Zhou, X. J.; Geng, S. S.; Sheng, X. L.; Jiang, S. B.; Sun, S. H.; Qin, C. F.; Zhou, Y. S. Adaptation of SARS-CoV-2 in BALB/c mice for testing vaccine efficacy. *Science* **2020**, *369* (6511), 1603–1607.
- (6) Gobeil, S. M. C.; Janowska, K.; McDowell, S.; Mansouri, K.; Parks, R.; Manne, K.; Stalls, V.; Kopp, M. F.; Henderson, R.; Edwards, R. J.; Haynes, B. F.; Acharya, P. D614G Mutation Alters SARS-CoV-2 Spike Conformation and Enhances Protease Cleavage at the S1/S2 Junction. *Cell Rep.* **2021**, *34* (2), 108630.
- (7) Grubaugh, N. D.; Hanage, W. P.; Rasmussen, A. L. Making Sense of Mutation: What D614G Means for the COVID-19 Pandemic Remains Unclear. *Cell* **2020**, *182* (4), 794–795.
- (8) Hou, Y. X. J.; Chiba, S.; Halfmann, P.; Ehre, C.; Kuroda, M.; Dinno, K. H.; Leist, S. R.; Schafer, A.; Nakajima, N.; Takahashi, K.; Lee, R. E.; Mascenik, T. M.; Graham, R.; Edwards, C. E.; Tse, L. V.; Okuda, K.; Markmann, A. J.; Bartelt, L.; de Silva, A.; Margolis, D. M.; Boucher, R. C.; Randell, S. H.; Suzuki, T.; Gralinski, L. E.; Kawaoka, Y.; Baric, R. S. SARS-CoV-2 D614G variant exhibits efficient replication ex vivo and transmission in vivo. *Science* **2020**, *370* (6523), 1464–1468.
- (9) Korber, B.; Fischer, W. M.; Gnanakaran, S.; Yoon, H.; Theiler, J.; Abfalterer, W.; Hengartner, N.; Giorgi, E. E.; Bhattacharya, T.; Foley, B.; Hastie, K. M.; Parker, M. D.; Partridge, D. G.; Evans, C. M.; Freeman, T. M.; de Silva, T. I.; McDaniel, C.; Perez, L. G.; Tang, H. L.; Moon-Walker, A.; Whelan, S. P.; LaBranche, C. C.; Saphire, E. O.; Montefiori, D. C.; Grp, S. C.-G.; et al. Tracking Changes in SARS-CoV-2 Spike: Evidence that D614G Increases Infectivity of the COVID-19 Virus. *Cell* **2020**, *182* (4), 812–827.
- (10) Yurkovetskiy, L.; Wang, X.; Pascal, K. E.; Tomkins-Tinch, C.; Nyalile, T.; Wang, Y. T.; Baum, A.; Diehl, W. E.; Dauphin, A.; Carbone, C.; Veinotte, K.; Egri, S. B.; Schaffner, S. F.; Lemieux, J. E.; Munro, J.; Rafique, A.; Barve, A.; Sabeti, P. C.; Kyratsous, C. A.; Dudkina, N.; Shen, K.; Luban, J. Structural and Functional Analysis of the D614G SARS-CoV-2 Spike Protein Variant. *Cell* **2020**, *183* (3), 739–751.
- (11) Hofmann, H.; Pohlmann, S. Cellular entry of the SARS coronavirus. *Trends Microbiol.* **2004**, *12* (10), 466–472.
- (12) Lu, G. W.; Wang, Q. H.; Gao, G. F. Bat-to-human: spike features determining 'host jump' of coronaviruses SARS-CoV, MERS-CoV, and beyond. *Trends Microbiol.* **2015**, *23* (8), 468–478.
- (13) Li, F. Structure, Function, and Evolution of Coronavirus Spike Proteins. *Annu. Rev. Virol.* **2016**, *3* (1), 237–261.
- (14) Hoffmann, M.; Kleine-Weber, H.; Schroeder, S.; Kruger, N.; Herrler, T.; Erichsen, S.; Schiergens, T. S.; Herrler, G.; Wu, N. H.; Nitsche, A.; Muller, M. A.; Drosten, C.; Pohlmann, S. SARS-CoV-2 Cell Entry Depends on ACE2 and TMPRSS2 and Is Blocked by a Clinically Proven Protease Inhibitor. *Cell* **2020**, *181* (2), 271–280.
- (15) Zhou, P.; Yang, X. L.; Wang, X. G.; Hu, B.; Zhang, L.; Zhang, W.; Si, H. R.; Zhu, Y.; Li, B.; Huang, C. L.; Chen, H. D.; Chen, J.; Luo, Y.; Guo, H.; Jiang, R. D.; Liu, M. Q.; Chen, Y.; Shen, X. R.; Wang, X.; Zheng, X. S.; Zhao, K.; Chen, Q. J.; Deng, F.; Liu, L. L.; Yan, B.; Zhan, F. X.; Wang, Y. Y.; Xiao, G. F.; Shi, Z. L. A pneumonia outbreak associated with a new coronavirus of probable bat origin. *Nature* **2020**, *579* (7798), 270–273.
- (16) Wang, Q. H.; Zhang, Y. F.; Wu, L. L.; Niu, S.; Song, C. L.; Zhang, Z. Y.; Lu, G. W.; Qiao, C. P.; Hu, Y.; Yuen, K. Y.; Wang, Q. S.; Zhou, H.; Yan, J. H.; Qi, J. X. Structural and Functional Basis of SARS-CoV-2 Entry by Using Human ACE2. *Cell* **2020**, *181* (4), 894–904.
- (17) Shang, J.; Ye, G.; Shi, K.; Wan, Y. S.; Luo, C. M.; Aihara, H.; Geng, Q. B.; Auerbach, A.; Li, F. Structural basis of receptor recognition by SARS-CoV-2. *Nature* **2020**, *581* (7807), 221–224.
- (18) Lan, J.; Ge, J. W.; Yu, J. F.; Shan, S. S.; Zhou, H.; Fan, S. L.; Zhang, Q.; Shi, X. L.; Wang, Q. S.; Zhang, L. Q.; Wang, X. Q. Structure of the SARS-CoV-2 spike receptor-binding domain bound to the ACE2 receptor. *Nature* **2020**, *581* (7807), 215–220.

- (19) Wang, Y. J.; Liu, M. Y.; Gao, J. L. Enhanced receptor binding of SARS-CoV-2 through networks of hydrogen-bonding and interactions. *Proc. Natl. Acad. Sci. U. S. A.* **2020**, *117* (25), 13967–13974.
- (20) He, J. H.; Tao, H. Y.; Yan, Y. M.; Huang, S. Y.; Xiao, Y. Molecular Mechanism of Evolution and Human Infection with SARS-CoV-2. *Viruses* **2020**, *12* (4), 428–438.
- (21) Amin, M.; Sorour, M. K.; Kasry, A. Comparing the Binding Interactions in the Receptor Binding Domains of SARS-CoV-2 and SARS-CoV. *J. Phys. Chem. Lett.* **2020**, *11* (12), 4897–4900.
- (22) Nguyen, H. L.; Lan, P. D.; Thai, N. Q.; Nissley, D. A.; O'Brien, E. P.; Li, M. S. Does SARS-CoV-2 Bind to Human ACE2 More Strongly Than Does SARS-CoV? *J. Phys. Chem. B* **2020**, *124* (34), 7336–7347.
- (23) Spinello, A.; Saltalamacchia, A.; Magistrato, A. Is the Rigidity of SARS-CoV-2 Spike Receptor-Binding Motif the Hallmark for Its Enhanced Infectivity? Insights from All-Atom Simulations. *J. Phys. Chem. Lett.* **2020**, *11* (12), 4785–4790.
- (24) Wrapp, D.; Wang, N. S.; Corbett, K. S.; Goldsmith, J. A.; Hsieh, C. L.; Abiona, O.; Graham, B. S.; McLellan, J. S. Cryo-EM structure of the 2019-nCoV spike in the prefusion conformation. *Science* **2020**, *367* (6483), 1260–1263.
- (25) Xu, C.; Wang, Y. X.; Liu, C. X.; Zhang, C.; Han, W. Y.; Hong, X. Y.; Wang, Y. F.; Hong, Q.; Wang, S. T.; Zhao, Q. Y.; Wang, Y. L.; Yang, Y.; Chen, K. J.; Zheng, W.; Kong, L. L.; Wang, F. F.; Zuo, Q. Y.; Huang, Z.; Cong, Y. Conformational dynamics of SARS-CoV-2 trimeric spike glycoprotein in complex with receptor ACE2 revealed by cryo-EM. *Science Advances* **2021**, *7* (1), eabe5575.
- (26) Peng, C.; Zhu, Z.; Shi, Y.; Wang, X.; Mu, K.; Yang, Y.; Zhang, X.; Xu, Z.; Zhu, W. Computational Insights into the Conformational Accessibility and Binding Strength of SARS-CoV-2 Spike Protein to Human Angiotensin-Converting Enzyme 2. *J. Phys. Chem. Lett.* **2020**, *11* (24), 10482–10488.
- (27) Hao, W.; Ma, B.; Li, Z.; Wang, X.; Gao, X.; Li, Y.; Qin, B.; Shang, S.; Cui, S.; Tan, Z. Binding of the SARS-CoV-2 spike protein to glycans. *Science Bulletin* **2021**, *66* (12), 1205–1214.
- (28) O'Callaghan, P.; Li, J. P.; Lannfelt, L.; Lindahl, U.; Zhang, X. Microglial Heparan Sulfate Proteoglycans Facilitate the Cluster-of-Differentiation 14 (CD14)/Toll-like Receptor 4 (TLR4)-Dependent Inflammatory Response. *J. Biol. Chem.* **2015**, *290* (24), 14904–14914.
- (29) Milewska, A.; Zarebski, M.; Nowak, P.; Stozek, K.; Potempa, J.; Pyrc, K. Human Coronavirus NL63 Utilizes Heparan Sulfate Proteoglycans for Attachment to Target Cells. *J. Virol.* **2014**, *88* (22), 13221–13230.
- (30) Cagno, V.; Tseligka, E. D.; Jones, S. T.; Tapparel, C. Heparan Sulfate Proteoglycans and Viral Attachment: True Receptors or Adaptation Bias? *Viruses* **2019**, *11* (7), 596–619.
- (31) Clausen, T. M.; Sandoval, D. R.; Spliid, C. B.; Pihl, J.; Perrett, H. R.; Painter, C. D.; Narayanan, A.; Majowicz, S. A.; Kwong, E. M.; McVicar, R. N.; Thacker, B. E.; Glass, C. A.; Yang, Z.; Torres, J. L.; Golden, G. J.; Bartels, P. L.; Porell, R. N.; Garretson, A. F.; Laubach, L.; Feldman, J.; Yin, X.; Pu, Y.; Hauser, B. M.; Caradonna, T. M.; Kellman, B. P.; Martino, C.; Gordts, P. L. S. M.; Chanda, S. K.; Schmidt, A. G.; Godula, K.; Leibel, S. L.; Jose, J.; Corbett, K. D.; Ward, A. B.; Carlin, A. F.; Esko, J. D. SARS-CoV-2 Infection Depends on Cellular Heparan Sulfate and ACE2. *Cell* **2020**, *183* (4), 1043–1057.
- (32) Zhang, Q.; Chen, C. Z.; Swaroop, M.; Xu, M.; Wang, L. H.; Lee, J.; Wang, A. Q.; Pradhan, M.; Hagen, N.; Chen, L.; Shen, M.; Luo, Z. J.; Xu, X.; Xu, Y.; Huang, W. W.; Zheng, W.; Ye, Y. H. Heparan sulfate assists SARS-CoV-2 in cell entry and can be targeted by approved drugs in vitro. *Cell Discovery* **2020**, *6* (1), 80–93.
- (33) Chu, H.; Hu, B.; Huang, X.; Chai, Y.; Zhou, D.; Wang, Y.; Shuai, H.; Yang, D.; Hou, Y.; Zhang, X.; Yuen, T. T.; Cai, J. P.; Zhang, A. J.; Zhou, J.; Yuan, S.; To, K. K.; Chan, I. H.; Sit, K. Y.; Foo, D. C.; Wong, I. Y.; Ng, A. T.; Cheung, T. T.; Law, S. Y.; Au, W. K.; Brindley, M. A.; Chen, Z.; Kok, K. H.; Chan, J. F.; Yuen, K. Y. Host and viral determinants for efficient SARS-CoV-2 infection of the human lung. *Nat. Commun.* **2021**, *12* (1), 134–148.
- (34) Nadir, Y.; Brenner, B. Relevance of Heparan Sulfate and Heparanase to Severity of COVID-19 in the Elderly. *Semin. Thromb. Hemostasis* **2021**, *47* (4), 348–350.
- (35) Drago, F.; Gozzo, L.; Li, L.; Stella, A.; Cosmi, B. Use of Enoxaparin to Counteract COVID-19 Infection and Reduce Thromboembolic Venous Complications: A Review of the Current Evidence. *Front. Pharmacol.* **2020**, *11*, 579886–579891.
- (36) Tegally, H.; Wilkinson, E.; Giovanetti, M.; Iranzadeh, A.; Fonseca, V.; Giandhari, J.; Doolabh, D.; Pillay, S.; San, E. J.; Msomi, N.; Mlisana, K.; von Gottberg, A.; Walaza, S.; Allam, M.; Ismail, A.; Mohale, T.; Glass, A. J.; Engelbrecht, S.; Van Zyl, G.; Preiser, W.; Petruccione, F.; Sigal, A.; Hardie, D.; Marais, G.; Hsiao, M.; Korsman, S.; Davies, M. A.; Tyers, L.; Mudau, I.; York, D.; Maslo, C.; Goedhals, D.; Abrahams, S.; Laguda-Akingba, O.; Alisoltani-Dehkordi, A.; Godzik, A.; Wibmer, C. K.; Sewell, B. T.; Lourenco, J.; Alcantara, L. C. J.; Kosakovsky Pond, S. L.; Weaver, S.; Martin, D.; Lessells, R. J.; Bhiman, J. N.; Williamson, C.; de Oliveira, T. Emergence of a SARS-CoV-2 variant of concern with mutations in spike glycoprotein. *Nature* **2021**, *592*, 438–443.
- (37) Khan, A.; Zia, T.; Suleman, M.; Khan, T.; Ali, S. S.; Abbasi, A. A.; Mohammad, A.; Wei, D. Q. Higher infectivity of the SARS-CoV-2 new variants is associated with K417N/T, E484K, and N501Y mutants: An insight from structural data. *J. Cell. Physiol.* **2021**, DOI: 10.1002/jcp.30367.
- (38) Zhou, D.; Dejnirattisai, W.; Supasa, P.; Liu, C.; Mentzer, A. J.; Ginn, H. M.; Zhao, Y.; Duyvesteyn, H. M. E.; Tuekprakhon, A.; Nutalai, R.; Wang, B.; Paesen, G. C.; Lopez-Camacho, C.; Slon-Campos, J.; Hallis, B.; Coombes, N.; Bewley, K.; Charlton, S.; Walter, T. S.; Skelly, D.; Lumley, S. F.; Dold, C.; Levin, R.; Dong, T.; Pollard, A. J.; Knight, J. C.; Crook, D.; Lambe, T.; Clutterbuck, E.; Bibi, S.; Flaxman, A.; Bittaye, M.; Belij-Rammerstorfer, S.; Gilbert, S.; James, W.; Carroll, M. W.; Klenerman, P.; Barnes, E.; Dunachie, S. J.; Fry, E. E.; Mongkolsapaya, J.; Ren, J.; Stuart, D. I.; Sreaton, G. R. Evidence of escape of SARS-CoV-2 variant B.1.351 from natural and vaccine-induced sera. *Cell* **2021**, *184* (9), 2348–2361.